photonics

MDPI

Article

Machine Learning-Assisted Analysis of Interferometric Optical Sensor Signals

Sergio Ivan Ramirez-Zavala, Ana Dinora Guzman-Chavez *, Everardo Vargas-Rodriguez *, José Carmen Morales-Castro and Juan José Paniagua-Medina

Departamento de Estudios Multidisciplinarios, División de Ingenierías, Campus Irapuato-Salamanca, Universidad de Guanajuato, Yuriria 38940, Guanajuato, Mexico; si.ramirezzavala@ugto.mx (S.I.R.-Z.); jc.moralescastro@ugto.mx (J.C.M.-C.); jj.paniaguamedina@ugto.mx (J.J.P.-M.)
* Correspondence: ad.guzman@ugto.mx (A.D.G.-C.); evr@ugto.mx (E.V.-R.)

Abstract

An analysis of interferometric optical temperature sensors based on machine learning methods is presented. Here, the signals are generated by two interferometric systems which were fabricated using stacked layers at the tip of an optical fiber. These systems are theoretically modeled and experimentally tested. For the theoretical model, the summation of rays reflected between interfaces was used. Besides, the thermal properties of the layers were considered to characterize the interferometers' response to temperature changes. In this work, the sensor that generates each signal was identified by means of the kernel linear discriminant analysis classification method. Later, the kernel ridge regression method was applied to determine the values of the physical parameter measured by each sensor. For both algorithms, the input features were extracted from the output optical spectra of the sensors, which capture changes in wavelength and amplitude. Here, it is shown that for the experimental test dataset, the achieved average accuracy of the classification, the root mean square error, the mean absolute error and the determination coefficient of the regression algorithms were 100%, 0.096 °C, 0.080 °C and 0.999, respectively.

Keywords: optical sensor; interference; temperature; kernel linear discriminant analysis; kernel ridge regression

1. Introduction

Optical sensors are widely studied due to characteristics such as high sensitivity, relatively easy fabrication, and immunity to electromagnetic interference. This category includes Fabry–Pérot interferometric optical sensors formed by cavities or layers of special materials deposited at the tip of an optical fiber. These devices utilize optical interference to convert environmental changes into detectable fringe patterns. Such changes may involve strain, temperature, and refractive index. For example, for simultaneous measurement of humidity and temperature, a sensor based on polymer-coated fiber cavities has been proposed [1]. The sensing element of that measuring device consisted of two polymer layers deposited at the end of a section of hollow core Bragg fiber which was spliced with a single-mode fiber pigtail. The layer materials were chitosan and an ultraviolet optical adhesive. In another interesting work, a highly sensitive MEMS Fabry–Pérot pressure sensor was proposed [2]. That sensor was formed by silicon, vacuum, and hybrid silicon-vacuum micro-cavities. In a further example, authors proposed an ultra-high sensitivity gas refractive index fiber sensor based on a Fabry–Pérot interferometer [3], which consisted

Check for updates

Received: 3 September 2026
Revised: 18 September 2026
Accepted: 29 September 2026
Published: 1 October 2026

Copyright: © 2026 by the authors. Licensee MDPI, Basel, Switzerland. This article is an open access article distributed under the terms and conditions of the Creative Commons Attribution (CC BY) license.

of a capillary tube spliced to a piece of photonic crystal fiber (PCF) and a section of single-mode fiber.

Traditionally, methods used to analyze signals from interferometric optical sensors limit the measurement ranges, as these cannot overcome the phase ambiguity inherent in the interference signal or the non-linear relationships between input variables and the output variable (the parameter being measured). To overcome these limitations, signal analysis using advanced data processing techniques has been proposed. In recent years, machine learning-based models have been widely adopted for estimation tasks through classification and regression methods. In interferometric optical sensors, these methods have allowed measurement range extension and have facilitated multiparameter sensing. For example, some works have used a classification approach [4–7] such as the support vector machine method, which has been used to identify refractive index variations from interference patterns generated by cascaded cavities [4]. Moreover, using this method, the measurement ambiguity between samples that represent refractive index values below and above the effective refractive index of the fundamental fiber mode was overcome. In another example, a vector-based pattern recognition algorithm was proposed to analyze different sensors that monitor refractive index, bending, and strain [7]. In that work, the authors used the angular similarity to determine the values of the parameter associated with the pattern. The advantage of these methods is their ability to recognize diverse and complex patterns; however, a key limitation is that a large database is required to achieve high precision and resolution, since performance is limited by the number of recorded signals available for comparison.

Regarding regression methods, they allow for continuous estimation directly from interferometric spectra [8–14]. For example, a sensing arrangement for the simultaneous measurement of temperature and strain with optical interferometers based on an artificial neural network has been reported in the literature [11]. In that system, an improvement in the root mean square error was achieved compared to that obtained with traditional methods. In another interesting example, a balloon-shaped optical fiber was used to implement a sensor in which the displacement was estimated using Gaussian process regression [13]. In that work, the authors emphasized that the machine learning-based approach used capitalizes on features extracted from measured spectra, overcoming the dynamic range limitations imposed by the conventional dip tracking method. Moreover, the advantage of these methods is that, with fewer samples, a mathematical relationship can be derived to estimate values that were not used for training, enabling estimates with higher resolution and precision.

Despite advances in methods to improve the analysis of interferometric optical sensors (IOSs), to the best of our knowledge, no combined classification–regression framework has been implemented for a comprehensive analysis of signals coming from different sensors. Motivated by this gap, in this work the implementation of a machine learning-based regression and classification framework is presented for the analysis of two different IOSs. The analyzed signals were obtained from two IOSs fabricated by depositing thin layers at the tip of an optical fiber. Moreover, these were theoretically modeled to obtain a robust spectral database. In particular, kernel linear discriminant analysis (KLDA) was used to identify the sensor from which the signal originated; subsequently, Kernel Ridge Regression (KRR) was applied to provide continuous temperature estimation over a wide measurement range. In addition, it is important to mention that the optimal hyperparameters were determined by applying the cross validation technique and that the input values of the implemented framework were a set of features extracted from the output interference spectra of the sensors. Furthermore, the accuracy, the root mean square error and the mean absolute error achieved were 100% and on the order of 10^{-2} °C, respectively.

2. Operating Principle of the Interferometric Optical Sensors

The physical configuration of the two interferometric optical sensors used for the analysis of their signals was based on a stack of thin infrared-transparent layers deposited at the tip of an optical fiber. The output signal from this type of sensor was an interference pattern resulting from the superposition of the individual interference patterns generated at each layer. This resulting signal can be modeled using the theory of summation of the principal rays reflected at the interfaces within the layer stack (Figure 1). For the specific case of an optical interferometer with two active layers, the reflected electric field can be expressed as

$$E_T = E_{F1} + E_{F2} + E_{F3}, \tag{1}$$

where E_{Fi} is the electric field reflected by the Fi-th interface. The electric field reflected by the first interface $F1$ is

$$E_{F1} = a_0 = E_0 r_1^+, \tag{2}$$

where E_0 is the input electric field and r_i is the Fresnel reflection coefficient. The sum of all the rays reflected by the second interface $F2$ is

$$\begin{aligned} E_{F2} =& b_1 + b_2 + b_3 + \ldots + b_n, \\ =& E_o l_1 t_1^+ t_1^- r_2^+ e^{i2\delta_1} \\ &+ E_o (l_1)^2 t_1^+ t_1^- (r_2^+)^2 r_1^- e^{i4\delta_1} \\ &+ E_o (l_1)^3 t_1^+ t_1^- (r_2^+)^3 (r_1^-)^2 e^{i6\delta_1} \\ &+ \ldots + E_o (l_1)^m t_1^+ t_1^- (r_2^+)^m (r_1^-)^{m-1} e^{i2m\delta_1} \\ =& E_o t_1^+ t_1^- \sum_{k=1}^{m} (l_1 r_2^+)^k (r_1^-)^{k-1} e^{i2k\delta_1}, \end{aligned} \tag{3}$$

where t_i is the Fresnel transmission coefficient, l_i represents the losses attributed to the i-th layer, and m is the number of times the reflected electric field is added per pass. In a multilayer thin-film optical system with interfaces of relatively low reflectance, higher-order multiple reflections can be neglected, and the summation can be truncated to include only the initial reflections, as these represent the dominant contribution to the total output intensity. Moreover, δ_i is the optical phase difference expressed as

$$\delta_i = 2\pi/\lambda n_i d_i, \tag{4}$$

where λ is the wavelength, and n_i and d_i are the refractive index and the thickness of the i-th layer, respectively. Now, the sum of all the rays reflected by the third interface $F3$ is given by

$$\begin{aligned} E_{F3} =& c_1 + c_2 + c_3 + \ldots + c_n \\ =& E_o l_1 l_2 t_1^+ t_2^+ t_1^- t_2^- r_3^+ e^{i(2\delta_1 + 2\delta_2)} \\ &+ E_o l_1 (l_2)^2 t_1^+ t_2^+ t_1^- t_2^- (r_3^+)^2 r_2^- e^{i(2\delta_1 + 4\delta_2)} \\ &+ E_o l_1 (l_2)^3 t_1^+ t_2^+ t_1^- t_2^- (r_3^+)^3 (r_2^-)^2 e^{i(2\delta_1 + 6\delta_2)} \\ &+ \ldots + E_o l_1 (l_2)^m t_1^+ t_2^+ t_1^- t_2^- (r_3^+)^m (r_2^-)^{m-1} e^{i(2\delta_1 + 2m\delta_2)}, \\ =& E_o l_1 t_1^+ t_2^+ t_1^- t_2^- \sum_{k=1}^{m} (l_2 r_3^+)^k (r_2^-)^{k-1} e^{i(2\delta_1 + 2k\delta_2)}. \end{aligned} \tag{5}$$

Afterward, by substituting Equations (2), (3), and (5) into Equation (1), the total output reflected electric field can be expressed as

$$\begin{aligned} E_T =& E_0 r_1^+ + E_o t_1^+ t_1^- \sum_{k=1}^{m} (l_1 r_2^+)^k (r_1^-)^{k-1} e^{i2k\delta_1} \\ &+ E_o l_1 t_1^+ t_2^+ t_1^- t_2^- \sum_{k=1}^{m} (l_2 r_3^+)^k (r_2^-)^{k-1} e^{i(2\delta_1 + 2k\delta_2)}, \end{aligned} \tag{6}$$

where, $r_i^+ = -r_i^- = (n_{i-1} - n_i)/(n_{i-1} + n_i)$ and $t_i^+ = t_i^- = (2n_{i-1})/(n_{i-1} + n_i)$. Here, it is important to clarify that this equality holds for normal incidence. Finally, the reflected relative intensity is expressed as $I = |E_T/E_o|^2$. In addition, when the layers exhibit thermal properties—specifically significant thermal expansion (γ_i) and thermo-optical coefficients (ρ_i)—the induced phase difference at each layer is given by

$$\delta_i = 2\pi/\lambda(n_i + \Delta n_i)(d_i + \Delta d_i) \tag{7}$$

where $\Delta n_i = \rho_i(T - T_o)$ and $\Delta d_i = d_i\gamma_i(T - T_o)$ are the changes in the refractive index and the thickness, respectively; T is the temperature and T_0 is the reference temperature.

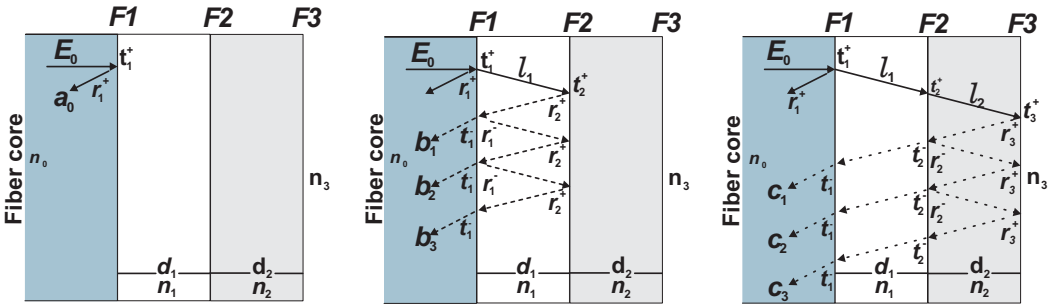


Figure 1. Waves reflected and transmitted occurring at each interface. The solid and dashed arrows represent the paths of the waves.

Physical Model and Experimental Setup

The interferometric optical sensors (IOS1 and IOS2) used for signal analysis were fabricated with two active layers, as shown in Figure 2a. Specifically, the layers L_1 and L_2 of IOS1 were air and cyanoacrylate, respectively. In IOS2, these layers were an anti-reflection coating and air. In both sensors, L_3 and L_4 were composed of stainless steel and epoxy resin, respectively. Consequently, as L_3 is not transparent to infrared light, it was not considered an active layer. In fact, this layer acts as a mirror and therefore it was used to increase reflectance at the third interface and prevent it from being affected by external factors. The fourth layer, which surrounds L_1 and L_2, acts as an external expander. Moreover, since L_4 has a high thermal expansion coefficient, it expands when its temperature increases, contributing to an increase in the thickness of L_2 in both sensors.

The experimental output signals were obtained by directing the light from a source to the interferometer through a circulator (Thorlabs 6015-3, Newton, NJ, USA). Here, the light source was an amplified spontaneous emission generated by means of a piece of erbium doped fiber (EDF, M5-980-125, Thorlabs, Newton, NJ, USA) of ≈3 m length, pumped with a diode laser emitting at 980 nm and delivering a maximum output power of 200 mW (Qphotonics QFBGLD-980-200, Ann Arbor, MI, USA). Afterwards, the reflected signal was routed back through the circulator and then captured by an Optical Spectrum Analyzer (OSA, Yokogawa AQ6370C, Tokyo, Japan) with a resolution of 0.2 nm (Figure 2b). Moreover, the OSA was set to acquire eight spectra and average them to get one overall spectrum. The sensor's temperature was changed by using a Thermo-Electric Cooler (TEC) driven

with a proportional–integral–derivative (PID) controller, which was implemented with an electronic stage based on a module (Maxim MAX8521, Sunnyvale, CA, USA) [15]. Here, we selected a temperature stabilization time of 10 min and it was monitored with a reference thermometer which was a digital thermometer for laboratory applications.

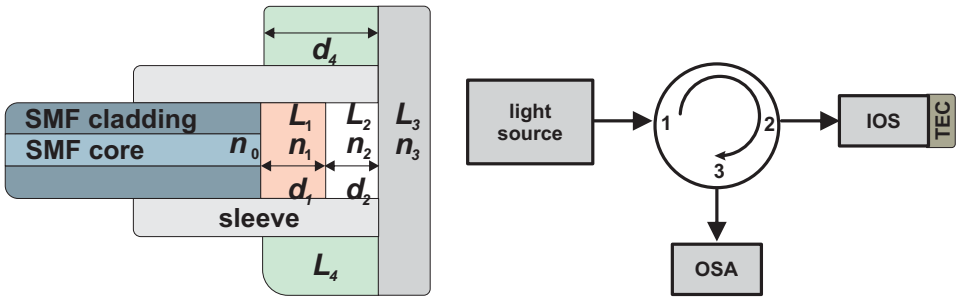


Figure 2. (**a**) Physical model of the IOS and (**b**) experimental setup for obtaining spectra at different temperatures.

3. Classification and Regression Models Used for the Analysis of Interferometric Optical Sensors

Classification and regression models were used for the analysis of interferometric optical sensors. For this analysis, the stages shown in Figure 3 were followed:

Stage 1. It consisted of extracting the features from the sensor's output spectrum. These features ($\mathbf{X} \leftarrow [\mathbf{x}_1\ \mathbf{x}_2\ \ldots\ \mathbf{x}_f] \in \mathbb{R}^{D\times f}$ where D and f are the number of cases and features, respectively) were used as input data for the algorithms implemented. In addition, the vector containing the class labels or temperature values of each sensor ($\mathbf{Y} \leftarrow [y_1\ y_2\ \ldots\ y_N]^T \in \mathbb{R}^{D\times 1}$) was used as input data.

Stage 2. It consisted of identifying the sensor from which the signal originated. The model used for this task was KLDA, which is a machine learning model designed for classification (Appendix A, Algorithm A1). This model uses the kernel trick to find an optimal projection space that separates groups that are linearly inseparable in their original input space [16]. Moreover, to implement this model, a set of hyperparameter values (z) must be defined for the kernel function ($k^z(\cdot,\cdot)$). This set of hyperparameters was optimized by performing a q-fold cross-validation. The main outputs of stage 2 included the accuracies (A^* and A_t), the confusion matrix ($\mathbf{S}$) and the vector containing the estimated class labels ($\hat{\mathbf{Y}}$). Here, the metric value with the subscript t is obtained for the test data, while the metric with an asterisk corresponds to the highest average accuracy calculated in the cross-validation process. Here, each average is calculated with the five values of each iteration of the cross-validation process.

Stage 3. It consisted of applying a model to estimate the temperature values measured by the source sensor identified in stage 2. Here, the KRR machine learning model was used to estimate these values (Appendix A, Algorithm A2). This model combines ridge regression with the kernel trick to find complex and nonlinear relationships in the data. The kernel trick enables the model to operate implicitly in a higher-dimensional feature space without explicitly projecting the data into it [17]. In addition to the input data from stage 1, a set of hyperparameter values (z) for the kernel function ($k^z(\cdot,\cdot)$) and a set of regularization parameter values (α) were used. These hyperparameter values were also optimized using q-fold cross-validation. The main outputs of stage 3 are the root mean square errors ($RMSE^*$ and $RMSE_t$), the mean absolute errors (MAE^* and MAE_t), the coefficients of determination ($(R^2)^*$ and $(R^2)_t$) and the vector containing the estimated temperature values ($\hat{\mathbf{Y}}$) . Here, the $RMSE^*$ value represents the lowest average calculated

from the five values of each iteration. Finally, the MAE^* and $(R^2)^*$ were computed using the hyperparameters associated with the $RMSE^*$ value.

As mentioned in Stage 2, the cross-validation technique was performed only with the training dataset. Moreover, to ensure model generalization, the features derived from the spectra must be randomly distributed across the training and validation folds. To control the random partitioning and ensure full reproducibility of the results, a pseudo-random seed was used. Additionally, each training and validation dataset was standardized using the mean and standard deviation of the training set. Later, these values were used to standardize the test dataset.

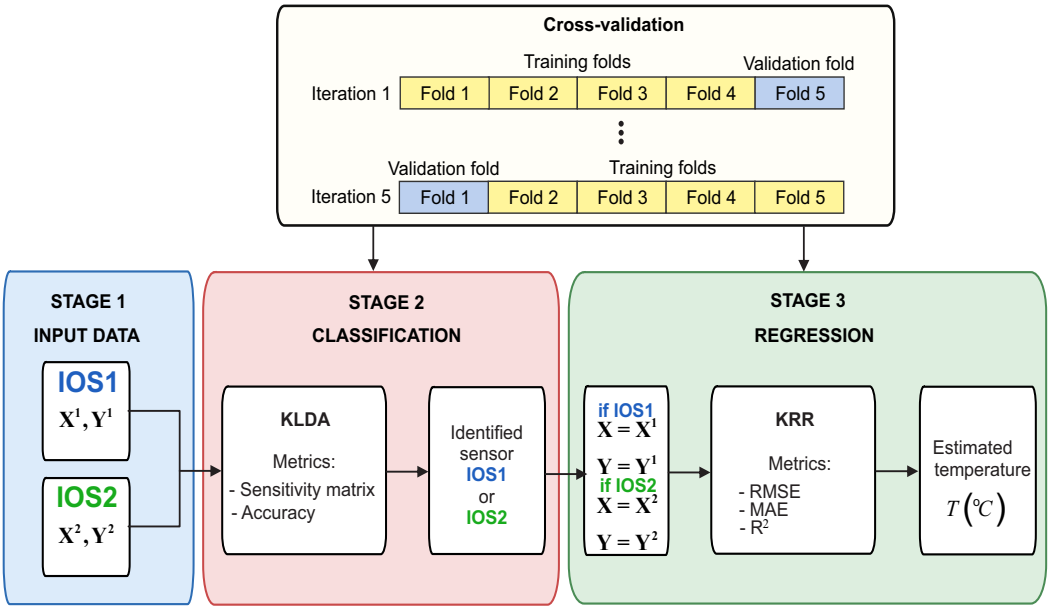


Figure 3. Workflow employed for sensor identification and temperature estimation.

4. Results

4.1. Theoretical Modeling of the Interferometric Optical Sensors

The simulated output spectra of IOS1 and IOS2 were obtained using the mathematical model described in Section 2. Here, the values used in the model were $m = 4$, $n_0 = 1.44$, $n_1 = 1.00$, $n_2 = 1.45$, $n_3 = 3.8$, $d_1 = 50.0$ µm, $d_2 = 1.78$ µm, $d_4 = 4190$ µm, $l_1 = 0.58$, and $l_2 = 0.45$ for IOS1 and $n_0 = 1.46$, $n_1 = 1.20$, $n_2 = 1.00$ and $n_3 = 3.8$, $d_1 = 0.325$ µm, $d_2 = 49.11$ µm, $d_4 = 4950$ µm $l_1 = 0.93$, and $l_2 = 0.96$ for IOS2. Besides, the thermo-optical coefficient of L_2 is $\rho_2 = -0.4 \times 10^{-4}$ K^{-1} and the thermal expansion coefficient of L_2 and L_4 are $\gamma_2 = 198$ µm/(m K) and $\gamma_4(T) = 2.9483 \times 10^{-4}(T - T_0)^3 + 1.1576 \times 10^{-2}(T - T_0)^2 + 0.8367(T - T_0) + 30.3419$ µm/(m °C), respectively. For the validation of the thermo-optic coefficients and refractive indices refer to [18,19]. Furthermore, due to the thermal properties of the epoxy clay, temperature increases cause it to expand. This thermal expansion leads to a separation between the sleeve and the stainless steel plate (Δd_4), thereby altering the thickness of L_2. Since d_2 is much smaller than L_4 and γ_4 is of the same order of magnitude as, or smaller than, that of L_2, the expansion of L_4 governs the thickness of the cavity L_2; consequently $\Delta d_2 = \Delta d_4$.

4.2. Manufacturing of the Interferometric Optical Sensors

Layer thicknesses were determined by controlling the separation between layers using a 3-axis stage and measuring the FSR of the reflected spectrum. The steps for manufacturing the filter were: 1. A piece of unused syringe needle (of 1.2 cm of length), which acts as a sleeve, was placed vertically over one of the surfaces of the stainless steel plate (L_3); 2. The

external expander with a length d_4 was formed around the syringe needle and it was glued to the stainless steel plate; 3. Once the EE was cured, the fiber for the IOS1 or the pigtailed ferrule for the IOS2 was introduced through the sleeve that was let uncovered, forming an air cavity; 4. The air cavity length was controlled by using a 3 axis stage and measuring the FSR2 $\approx \lambda^2/(2n_2d_2)$ from the measured spectrum; 5. The cyanoacrylate polymer (L_2 for IOS2) was deposited over the fiber through the sleeve, allowing the polymer to flow until the air cavity between the stainless steel plate and the fiber surfaces was filled. In this case, specifically for ISO1, cyanoacrylate was not allowed to flow. The thickness of the external expander was measured using a precision micrometer. After the thickness and refractive index of each layer were known, the l_i constants were calculated by minimizing a cost function that quantifies the discrepancy between the experimental and theoretical spectra [19].

It is important to point out that the proposed framework for identifying the sensor that generates the signal and estimates its temperature can be validated using only synthetic data such as those obtained with analytical models (as described in Section 2). However, in order to be able to test our framework with real experimental data two sensors were fabricated, following the manufacturing procedure described in the present section. Hence, the analytical model was useful for building a comprehensive synthetic dataset and to get a detailed insight of the dynamics of the filter performance as temperature changes. In addition, it allowed us to validate, in general terms, the experimentally measured spectra since these present a high agreement with the simulated ones, as can be appreciated in Figure 4. For both interferometers, 24 experimental spectra were recorded in temperature ranges between 24 and 37 °C for IOS1 and between 22 and 49 °C for IOS2.

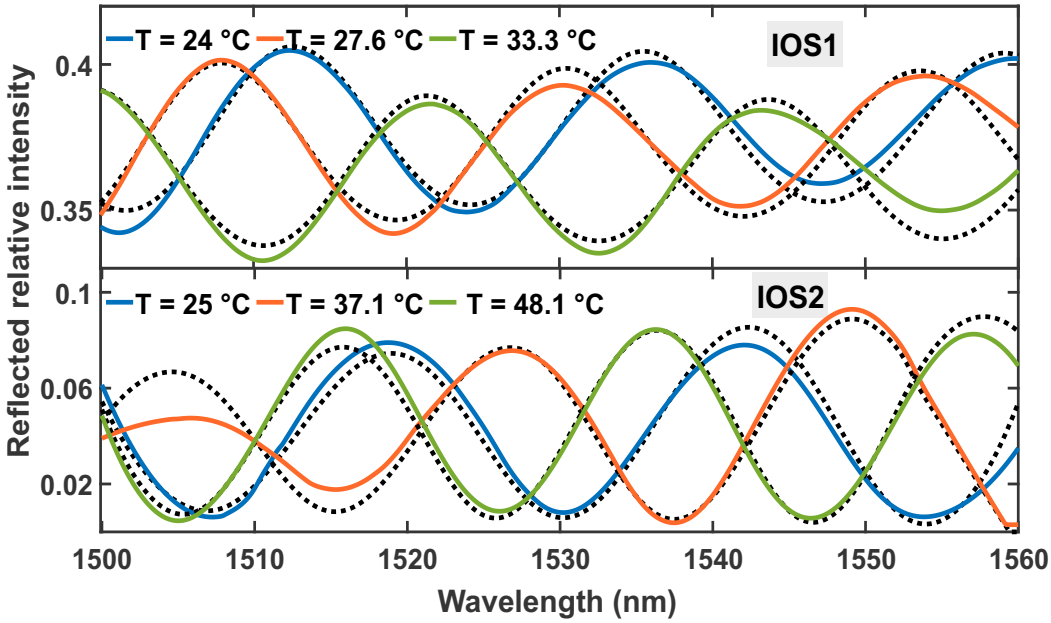


Figure 4. Experimental (solid lines) and simulated (dotted lines) spectra at different temperatures.

4.3. Synthetic Dataset for Validating the Machine Learning Framework

A total of $D = 501$ spectra were simulated to obtain a synthetic dataset to initially train and test the proposed machine learning framework. The synthetic dataset was formed with twenty features extracted from the spectra. To extract the features, each spectrum was divided into four spectral regions, 1500 to 1515 nm, 1516 to 1530 nm, 1531 to 1545 nm, and 1546 to 1560 nm. For each region, five features were obtained: the arithmetic mean (f_1), the wavelength and amplitude of the maximum peak (f_2 and f_3), the slope of the linear regression (f_4) and the percentile range (f_5), which was calculated as the difference

between the 90 and 10 percentiles of the amplitude. In this sense, the datasets for each sensor were the matrix $\mathbf{X} \in \mathbb{R}^{501\times20}$ and the vector $\mathbf{Y} \in \mathbb{R}^{501\times1}$. Finally, it is important to mention that the partition of the spectrum into distinct sub-bands allows us to extract unique information from each region. We decided to divide the spectrum into four intervals of equal spectral width to capture diverse spectral signatures and maximize the amount of information via features available for estimation.

In Figure 5, the features of two spectral regions are shown as a function of temperature. The features in the left column are those extracted from the first region of the IOS1 signals, while those in the right column are extracted from the third region of the IOS2 signals. It can be observed that if a single feature is used as an input variable to estimate the temperature, the measurement range would be limited to a range smaller than the temperature range required to shift the signals by one FSR (23 nm for IOS1 and 22 nm for IOS2), which is narrower than the operating range. This single-variable estimation approach is typical of traditional methods, such as conventional fringe or peak tracking, cross-correlation, and FFT-based estimation. Consequently, a multi-input model is required to estimate the measured parameter across the entire operating range. In this sense, if a larger set of features is utilized to cover the entire measurement range, methods lacking a kernel framework, such as ordinary ridge regression and linear support vector regression, would lead to underfitting. This occurs because the inherent non-linearity of the spectral features (behavior shown in Figure 5) significantly contributes to a non-linear relationship between these inputs and the output variable. The comparison between these methods is shown in Table 1. In this sense, given the nonlinear relationships within this range, kernel functions are necessary to capture the nonlinearities exhibited by the sensors and ensure accurate estimation across the entire spectrum. Additionally, it should be noted that if a model capable of processing this information is not used, it is difficult to identify the source of the signals. In this regard, KLDA and KRR machine learning models are proposed to classify the signals and estimate the temperature of both IOSs over a wide measurement range.

Table 1. Comparison of traditional and machine learning methods for the analysis of interferometric optical sensor signals.

Method	Measurement Range	Modeling Performance
Traditional methods (conventional fringe or peak tracking, cross-correlation, and FFT-based estimation)	$\leq$1 FSR	Ambiguity errors beyond 1 FSR
Multiple linear regression models (for example, ordinary ridge regression and linear support vector regression)	$\geq$1 FSR	Inability to capture non-linear relationship
Multiple linear regression models with kernels (for example, kernel ridge regression)	$\geq$1 FSR	High flexibility to map complex non-linear dynamics and multi-dimensional feature spaces.

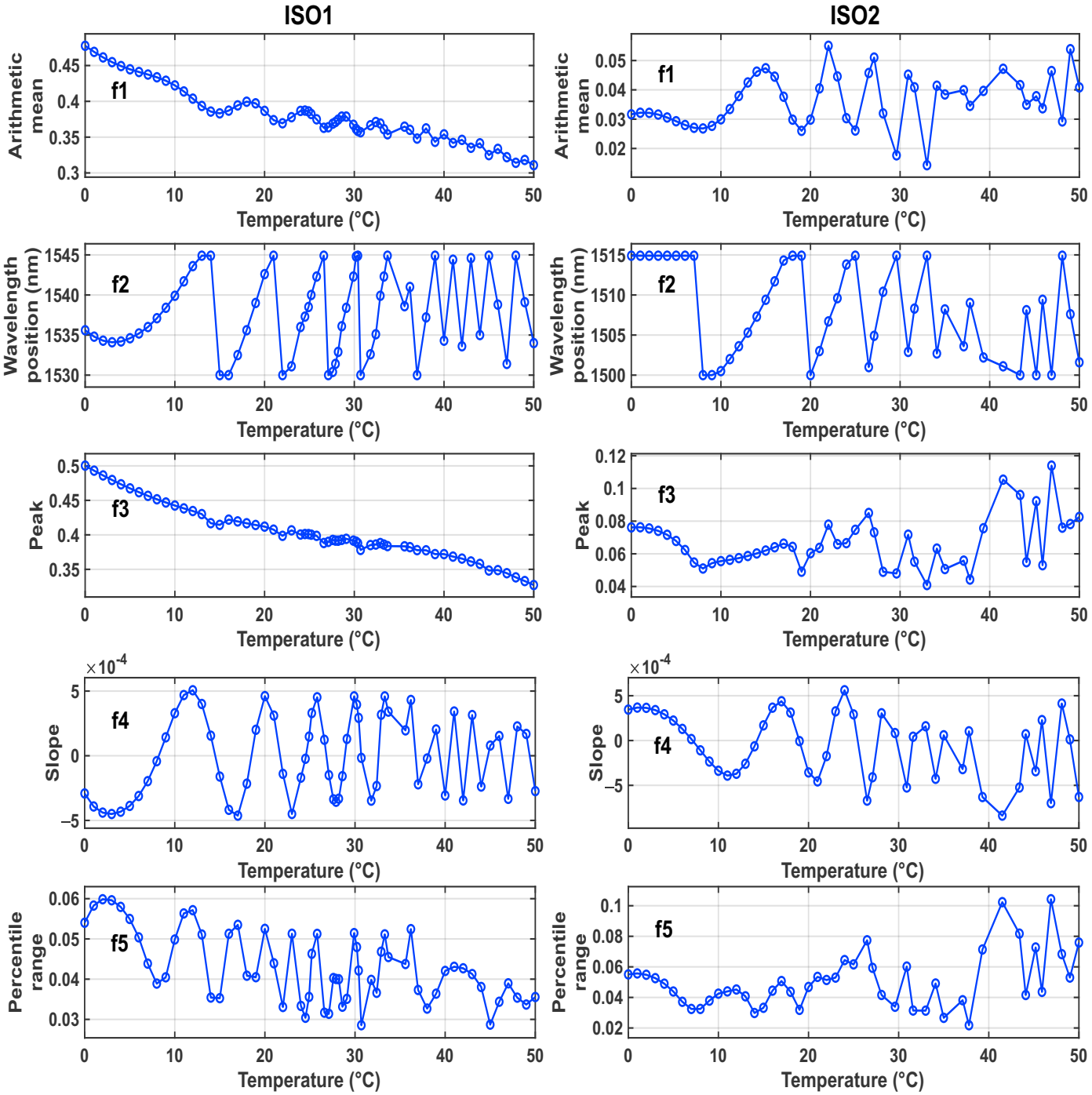


Figure 5. Evolution of the feature values as a function of the temperature.

4.3.1. Classification of the Sensor Source by Using the Simulated IOSs Data

The KLDA model was implemented in the classification stage, utilizing the input vectors $\mathbf{X}^1$, $\mathbf{X}^2$, $\mathbf{Y}^1$ and $\mathbf{Y}^2$. The entries of $\mathbf{Y}^1$ and $\mathbf{Y}^2$ were assigned values of 1 and 2, corresponding to IOS1 and IOS2, respectively. Besides, two kernel functions were tested, a linear kernel $k^z(\mathbf{x_i},\mathbf{x_j}) = (z+\mathbf{x_i}^T\mathbf{x_j})$ and a nonlinear kernel, a Gaussian kernel $k(\mathbf{x_i},\mathbf{x_j}) = \exp\left[-\|\mathbf{x_i}-\mathbf{x_j}\|^2/(2z^2)\right]$, in which $\mathbf{x_i}$ and $\mathbf{x_j}$ are column vectors. The z values were defined from 0 to 30 in increments of $m = 0.5$ for the linear kernel and from 0.2 to 50 in increments of $m = 0.1$ for the Gaussian kernel. Moreover, to apply the cross-validation technique, $q = 5$ folds were used. The optimal values obtained for the hyperparameters z^* are listed in Table 2.

In Figure 6a, the results obtained with the synthetic data are shown. Here, it can be observed that with the linear kernel, in which operations are performed directly in the original data space, the cases associated with each IOS cannot be fully separated with the optimal decision threshold b^*, reaching only an $A^* = 74.71\%$ and $A_t = 57.84\%$ (Table 3). In contrast, with the Gaussian kernel by means of which the data are implicitly projected into a higher dimensional space for linear separation, the cases can be classified with an $A^* = A_t = 100\%$ (Table 3). In Figure 6c, it can be seen that the cases associated with IOS1 and IOS2 are to the left and right of b^*, respectively. These results are also corroborated with the confusion matrix, since for the linear kernel the number of false IOS1 and IOS2 cases is high (Figure 6b), while for the Gaussian kernel the number of false cases is zero (Figure 6d).

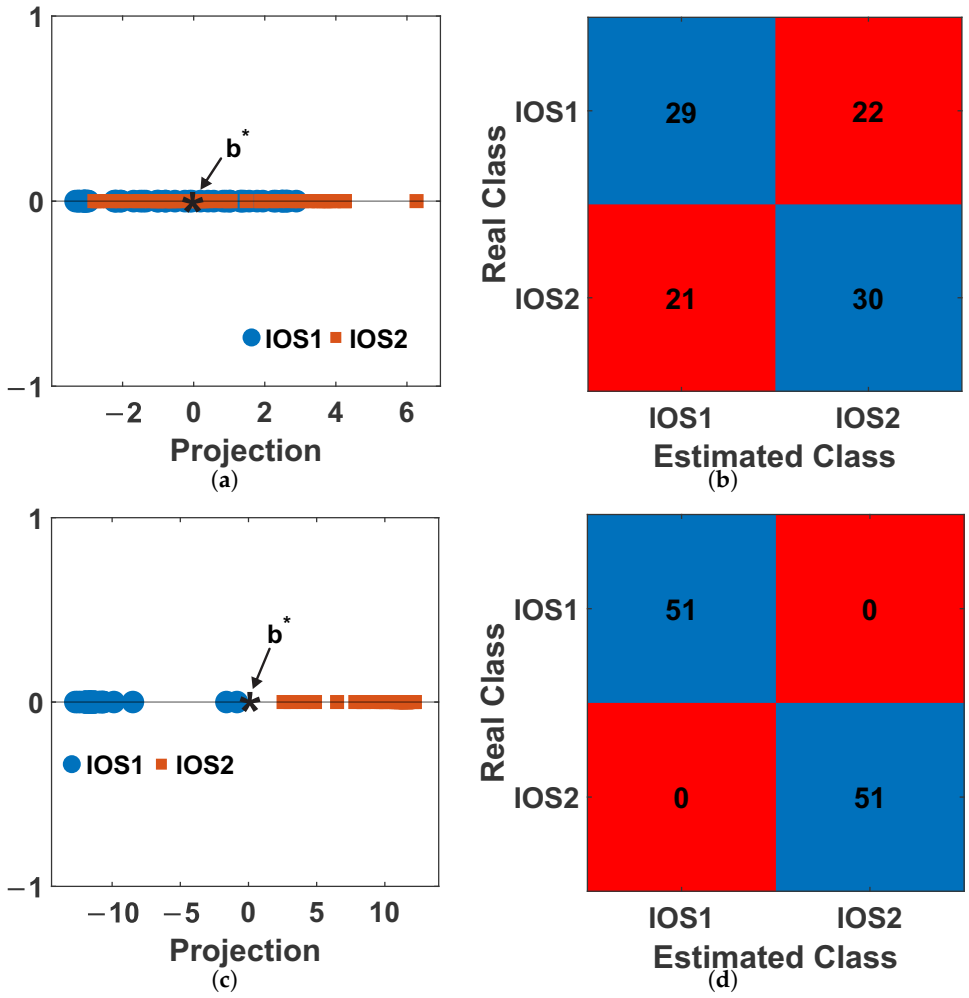


Figure 6. Classification results with (**a**) a linear and (**c**) a Gaussian kernel. Confusion matrix results using (**b**) a linear kernel and (**d**) a Gaussian kernel.

Table 2. Optimal hyperparameters obtained for IOS1 and IOS2 during the cross-validation stage. Linear kernel (LK) and Gaussian kernel (GK).

Method	**Case**	**Kernel**	z^* **LK:z = 0:0.5:30 GK:z = 0:0.1:15**	α^*
KLDA	IOS1–IOS2	Linear	0	–
		Gaussian	0.46	–

Table 2. *Cont.*

Method	Case	Kernel	z^* LK:z = 0:0.5:30 GK:z = 0:0.1:15	α^*
KRR	IOS1	Linear	3.8	1.18×10^{-12}
		Gaussian	4.3	5.08×10^{-5}
	IOS2	Linear	8.9	1.18×10^{-12}
		Gaussian	10	1.88×10^{-6}

Table 3. Metric values obtained for IOS1 and IOS2.

Method	Case	Kernel	Metric (Cross Validation)	Metric (Test Data)
KLDA	IOS1–IOS2	Linear	$A^* = 74.71\%$	$A_t = 57.84\%$
		Gaussian	$A^* = 100\%$	$A_t = 100\%$
KRR	IOS1	Linear	$RMSE^* = 1.973$ °C $MAE^* = 1.565$ °C $(R^2)^* = 0.981$	$RMSE_t = 2.209$ °C $MAE_t = 1.871$ °C $(R^2)_t = 0.973$
		Gaussian	$RMSE^* = 0.036$ °C [0.031, 0.042] – – – – – – $MAE^* = 0.025$ °C [0.025, 0.030] – – – – – – $(R^2)^* = 0.999$	$RMSE_t = 0.066$ °C [0.036, 0.094] – – – – – – $MAE_t = 0.047$ °C [0.024, 0.075] – – – – – – $(R^2)_t = 0.999$
	IOS2	Linear	$RMSE^* = 8.532$ °C $MAE^* = 6.404$ °C $(R^2)^* = 0.652$	$RMSE_t = 7.373$ °C $MAE_t = 6.155$ °C $(R^2)_t = 0.701$
		Gaussian	$RMSE^* = 0.026$ °C [0.023, 0.029] – – – – – – $MAE^* = 0.019$ °C [0.017, 0.022] – – – – – – $(R^2)^* = 0.99$	$RMSE_t = 0.056$ °C [0.025, 0.091] – – – – – – $MAE_t = 0.038$ °C [0.019, 0.064] – – – – – – $(R^2)_t = 0.999$

4.3.2. Temperature Estimation Using Simulated IOSs Data

To estimate the temperature of the IOS, the KRR regression model was implemented. Here, the input matrix and the vector for each sensor were **X** and **Y**, respectively. Moreover, the elements of **Y** were the temperature values. Here, linear and Gaussian kernel functions were tested, with the same set of z values used for classification, to determine which is the best for this application. In addition, to implement the KRR model, another set of input values α was defined as $\alpha_{i+1} = \alpha_i/3$, where $\alpha_{i=1} = 1$. Subsequently, a 5-fold cross-validation technique was applied to obtain the optimal hyperparameter values z^* and α^*, which are listed in Table 2. In Figure 7a,b, it is shown that with the linear kernel for both sensors (blue circles), the estimated values do not fit the real values, reaching an $RMSE^*$ of 1.973 °C and 8.532 °C; and an $RMSE_t$ of 2.209 °C and 7.373 °C for IOS1 and IOS2, respectively. The values for all metrics and their confidence intervals are shown in Table 3. In contrast, with the Gaussian kernel (red circles), good estimates were obtained, reaching a $RMSE^*$ of 0.038 °C and 0.026 °C; and an $RMSE_t$ of 0.065 °C and 0.056 °C for IOS1 and IOS2, respectively. Furthermore, with the results obtained with the nonlinear

kernel, the 95% confidence intervals were computed using 1000 samples of size 95 and 10, taken from the datasets containing 90% and 10% of the data, respectively. These samples were obtained using random sampling with replacement (Table 3).

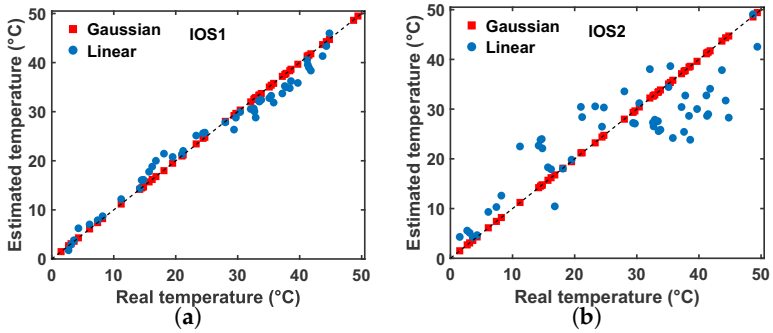


Figure 7. Regression results with both kernel functions for (**a**) the IOS1 and (**b**) the IOS2. The dashed lines represent the ideal estimation scenario.

4.4. Sensor Source Classification and Estimation of Its Temperature Using Experimental Data

To apply the proposed framework to the experimental IOS data, the experimental dataset was built following the same procedure as for the synthetic dataset. Later, this experimental dataset was augmented by interpolating the extracted features of each IOS. This allowed us to capture the actual dynamics of the sensor response to temperature variations. Moreover, the test dataset for each sensor was formed with 30% of the experimental registers while the training dataset was built with the remaining data. In this way, the datasets for each sensor can be expressed by the matrix $\mathbf{X} \in \mathbb{R}^{70\times 20}$ and the output vector $\mathbf{Y} \in \mathbb{R}^{70\times 1}$. These were used to execute the stages of the proposed framework, described in Section 3. Here, it is important to mention that we employed the Gaussian kernel, since—according to the results obtained with the synthetic data—it is the best option for our application. Moreover, after executing the steps of stage 1, it was obtained that $z^* = 0.46$ was the optimal hyperparameter for the classification model. With this value, the model achieved average sensor classification accuracies of $A^* = 94.62\%$ and $A_t = 100\%$ for the cross-validation procedure and test dataset, respectively (Figure 8). After executing stage 3 of the framework with the training experimental dataset, it was found that the optimal hyperparameters for the regression model for IOS1 were $z^* = 48.9$ and $\alpha^* = 1.88 \times 10^{-6}$, while for IOS2 were $z^* = 50.0$, and $\alpha^* = 3.18 \times 10^{-6}$. The list of metrics obtained by using these hyperparameters are listed in Table 4. In addition, Figure 8 displays the results obtained in both the classification and regression stages. Here, it can be observed that regression model fits with high precision both the training and the test experimental data of the two sensors.

Table 4. Hyperparameter and metric values obtained for IOS1 and IOS2 using experimental data.

Method	Case	Hyperparameters	Metric (Cross Validation Data)	Metric (Test Data)
KLDA	IOS1–IOS2	$z^* = 0.46$	$A^* = 94.62\%$	$A_t = 100\%$
KRR	IOS1	$z^* = 48.9$ $\alpha^* = 1.88 \times 10^{-6}$	$RMSE^* = 0.027$ °C $MAE^* = 0.203$ °C $(R^2)^* = 0.999$	$RMSE_t = 0.072$ °C $MAE_t = 0.063$ °C $(R^2)_t = 0.999$ °C
	IOS2	$z^* = 50$ $\alpha^* = 1.88 \times 10^{-6}$	$RMSE^* = 0.0041$ °C $MAE^* = 0.002$ °C $(R^2)^* = 0.99$	$RMSE_t = 0.121$ °C $MAE_t = 0.098$ °C $(R^2)_t = 0.999$

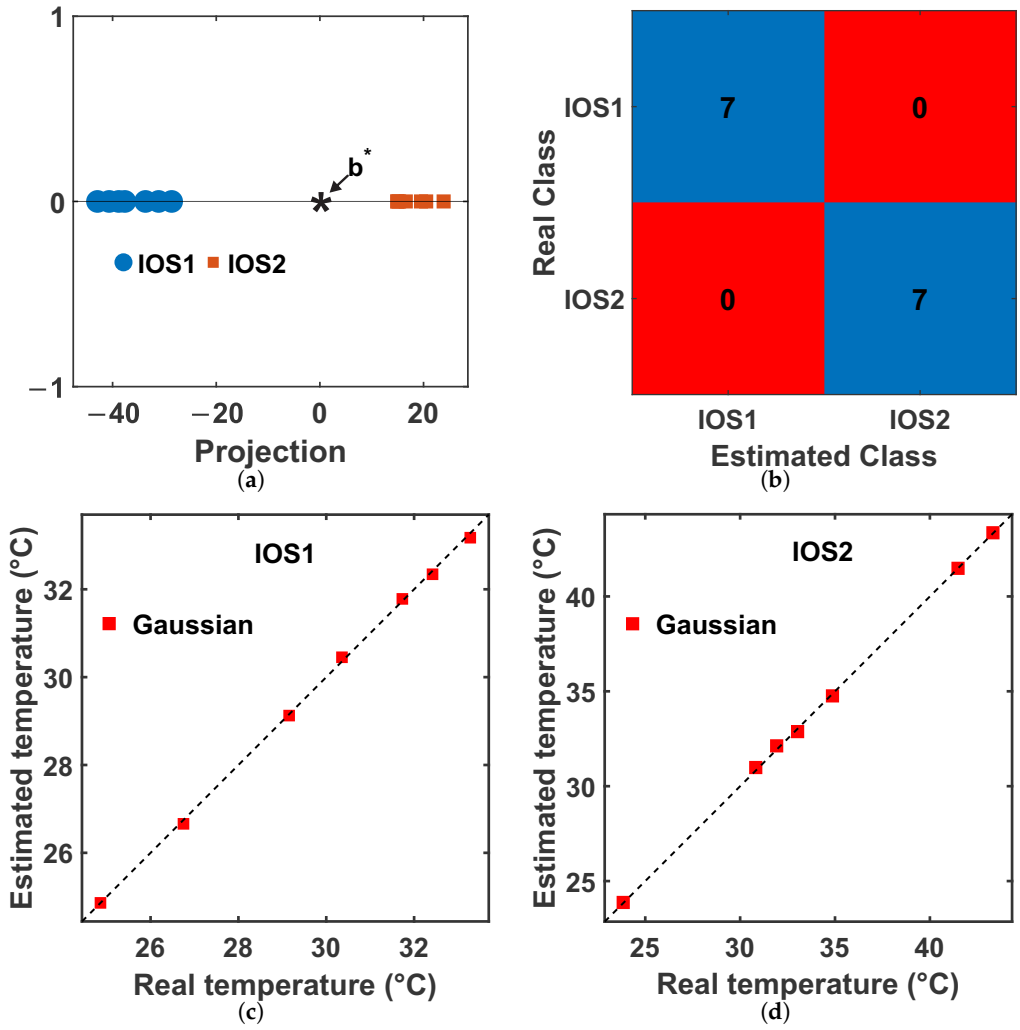


Figure 8. Classification and regression results for the experimental IOS data using a Gaussian kernel: (**a**) classification results (**c**) confusion matrix for the classification stage (**b**) regression results for IOS1 and (**d**) regression results for IOS2. The dashed lines represent the ideal estimation scenario.

5. Discussions

When dealing with nonlinear relationships between input variables (the features extracted from the sensor signals) and the measured parameter, combining linear discriminant analysis and ridge regression with nonlinear kernel functions yields highly effective signal analysis. With respect to the signal classification stage, it is important to emphasize that this stage can serve as an automated validation step in real-world scenarios where it is needed to identify the sensor that generates a particular spectrum such as automated sensor networks or decentralized testing environments: situations where human intervention is logistically unfeasible or prone to error. Regarding the regression stage, it is important to note that unlike the traditional linear regression method, kernel ridge regression is highly robust to collinearity due to its L2 regularization mechanism (the penalty term α), which prevents overfitting and ensures stable estimates even when using a robust set of features. This framework enables sensor identification in classification tasks and accurate temperature estimation across the entire operating range in regression tasks.

The results with synthetic data demonstrate the strong generalization capability of the model and the absence of overfitting. This is evidenced by comparing the metrics obtained via cross-validation with those from the independent test set. Furthermore, specifically regarding the regression stage, the fact that the metric values and their confidence intervals obtained with the test data closely align with those from the training and validation

data, falling within the same order of magnitude, confirms that the model maintains stable predictive performance on unseen data. Finally, implementing the framework with synthetic data was also useful to identify which kernel is best for this type of application since the behavior of the simulated spectrum is quite similar to the experimentally measured spectrum. Finally, the proposed methodology with the Gaussian kernel was executed again using the experimental data, and the obtained results demonstrated that the sensors were classified correctly and the temperature was estimated with high precision.

6. Conclusions

This work presents an analysis of signals from interferometric optical sensors (IOSs) using classification and regression machine learning models. Using the theory of the summation of the principal rays reflected between the layers, it was possible to model IOSs theoretically. This allowed us to build a comprehensive synthetic dataset that allowed us to evaluate the performance of the proposed framework for different hyperparameters and kernels. Moreover, it allowed us to support, in general terms, the experimental spectra, since these present a high agreement with the simulated spectra. After fitting the model to a synthetic dataset, it was found that the Gaussian kernel was the best for this application. Later, the model, with Gaussian kernels, was fitted again with the training part of the experimental data. Finally, for the experimental test data, it was obtained that using KLDA the sensor that generates the spectrum was identified with an accuracy of 100%. Furthermore, by applying KRR, the temperature was estimated with a mean square error, mean absolute error, and determination coefficient of 0.072 °C, 0.063 °C, and 0.999, respectively, for sensor 1; while for sensor 2 the same values were 0.121 °C, 0.098 °C, and 0.999. Moreover, it was demonstrated that the proposed framework allowed us to perform an ambiguity-free estimation over a wide measurement range. Finally, the combined use of KLDA and KRR enables the management of multiple IOSs. Moreover, the methodology is general, and we consider that it can be easily extended to other interferometric sensor configurations or to the simultaneous estimation of additional physical parameters.

Author Contributions: Conceptualization, S.I.R.-Z., A.D.G.-C. and E.V.-R.; methodology, S.I.R.-Z. and A.D.G.-C.; software, S.I.R.-Z., J.C.M.-C. and J.J.P.-M. ; formal analysis, S.I.R.-Z. and A.D.G.-C.; investigation, A.D.G.-C. and E.V.-R.; resources, S.I.R.-Z., A.D.G.-C. and E.V.-R.; data curation, J.C.M.-C. and J.J.P.-M.; writing—original draft preparation, S.I.R.-Z. and A.D.G.-C.; writing—review and editing, E.V.-R., J.C.M.-C. and J.J.P.-M.; funding acquisition, A.D.G.-C. and E.V.-R. All authors have read and agreed to the published version of the manuscript.

Funding: S.I. Ramirez-Zavala is grateful to the Secretaría de Ciencia, Humanidades, Tecnología e Innovación de México (SECIHTI), for the provided student research grant under number 1230247.

Institutional Review Board Statement: Not applicable.

Informed Consent Statement: Not applicable.

Data Availability Statement: The data supporting the findings of this study are available from the corresponding author upon reasonable request.

Conflicts of Interest: The authors declare no conflicts of interest.

Appendix A

Algorithm A1 Used to classify IOSs

Require: $\mathbf{X}^1, \mathbf{X}^2, \mathbf{Y}^1, \mathbf{Y}^2, z, k^z(\cdot,\cdot)$
Ensure: $z^*, \hat{\mathbf{Y}}, A^*, A_t, \mathbf{S}$

$q = 5, \mathbf{X} \leftarrow [\mathbf{X}^1 + \mathbf{X}^2]^T, \mathbf{Y} \leftarrow [\mathbf{Y}^1 + \mathbf{Y}^2]^T$.
$(\mathbf{X}, \mathbf{Y}) \xrightarrow{90/10\ \text{split}} [(\mathbf{X}_{TR}, \mathbf{Y}_{TR}), (\mathbf{X}_{TS}, \mathbf{Y}_{TS})]$.
$\mathbf{X}_{TR} \xrightarrow{\text{q-fold}} [\mathbf{fold}_1^{\mathbf{X}}\ \mathbf{fold}_2^{\mathbf{X}}\ \ldots\ \mathbf{fold}_q^{\mathbf{X}}]^T$.
$\mathbf{Y}_{TR} \xrightarrow{\text{q-fold}} [\mathbf{fold}_1^{\mathbf{Y}}\ \mathbf{fold}_2^{\mathbf{Y}}\ \ldots\ \mathbf{fold}_q^{\mathbf{Y}}]^T$.
for each $z \in \{0, m, 2m, \ldots, 1\}$ **do**
  $\mathbf{A}_z \leftarrow [\,]$; $\mathbf{b}_z \leftarrow [\,]$; $A_z \leftarrow 0$; $b_z \leftarrow 0$.
  for each $s \in \{1, 2, \ldots, q\}$ **do**
    $\mathbf{X}^{tr} \leftarrow \cup_{j \neq s} (\mathbf{fold}_j^{\mathbf{X}})^T$; $\mathbf{X}^{ts} \leftarrow (\mathbf{fold}_s^{\mathbf{X}})^T$.
    $\mathbf{Y}^{tr} \leftarrow \cup_{j \neq s} (\mathbf{fold}_j^{\mathbf{Y}})^T$; $\mathbf{Y}^{ts} \leftarrow (\mathbf{fold}_s^{\mathbf{Y}})^T$.
    $\mathbf{X}^{tr} \leftarrow \left(\dfrac{\mathbf{X}^{tr} - \text{mean}(\mathbf{X}^{tr})}{\text{std}(\mathbf{X}^{tr})}\right)^T$;
    $\mathbf{X}^{ts} \leftarrow \left(\dfrac{\mathbf{X}^{ts} - \text{mean}(\mathbf{X}^{tr})}{\text{std}(\mathbf{X}^{tr})}\right)^T$.
    $\text{Acc}^s \leftarrow 0, b^s \leftarrow 0, \hat{\mathbf{Y}}^s \leftarrow [\,], \hat{\mathbf{Y}} \leftarrow [\,]$.
    $(\mathbf{K})_{nm} \leftarrow k^z(\mathbf{x}_n^{tr}, \mathbf{x}_m^{tr})$.
    $\widetilde{\mathbf{K}} \leftarrow \mathbf{K} - \dfrac{q}{8(0.9D)}\mathbf{1}\mathbf{K} - \mathbf{K}\dfrac{q}{8(0.9D)}\mathbf{1} + \dfrac{q^2}{[8(0.9D)]^2}\mathbf{1}\mathbf{K}\mathbf{1}$.
    $\widetilde{\mathbf{K}}_1 \leftarrow \mathbf{K}_{2(0.9D)\times(1:(0.9D))}$;
    $\widetilde{\mathbf{K}}_2 \leftarrow \mathbf{K}_{2(0.9D)\times((0.9D)+1:2(0.9D))}$.
    $(\mathbf{M}_1)_j \leftarrow \dfrac{q(0.9D)}{4}\sum_{\mathbf{x}^{\mathbf{tr}^1} \in IOS1} k^z(\mathbf{x}_j^{tr}, \mathbf{x}^{\mathbf{tr}^1})$.
    $(\mathbf{M}_2)_j \leftarrow \dfrac{q(0.9D)}{4}\sum_{\mathbf{x}^{\mathbf{tr}^2} \in IOS2} k^z(\mathbf{x}_j^{tr}, \mathbf{x}^{\mathbf{tr}^2})$.
    $\mathbf{N} \leftarrow \sum_{i=1}^{2} \widetilde{\mathbf{K}}_i \left(\mathbf{I} - \dfrac{q(0.9D)}{4}\mathbf{1}\right) \widetilde{\mathbf{K}}_i^T$.
    $\mathbf{w} \leftarrow (\mathbf{N} + 0.01\mathbf{I})^{-1}(\mathbf{M}_2 - \mathbf{M}_1)$.
    for each $\mathbf{x} \in \mathbf{X}^{tr}$ **do**
      $p(\mathbf{x}^{tr}) \leftarrow \mathbf{w}^T k^z(\mathbf{x}^{tr}, \mathbf{x}^{ts})$.
    end for
    $b^s \leftarrow \dfrac{q}{8(0.9D)}\left(\sum_{\mathbf{x}^{tr} \in IOS1} p(\mathbf{x}^{tr}) + \sum_{\mathbf{x}^{tr} \in IOS2} p(\mathbf{x}^{tr})\right)$.
    for each $\mathbf{x} \in \mathbf{X}^{ts}$ **do**
      $\widetilde{k}^z(\mathbf{x}^{ts}) = k^z(\mathbf{X}^{tr}, \mathbf{x}^{ts}) - \dfrac{q}{8(0.9D)}\widetilde{\mathbf{K}}\mathbf{1}_{\frac{8(0.9D)}{q}\times 1}$
      $- \dfrac{q}{8(0.9D)}\mathbf{1}_{\frac{8(0.9D)}{q}\times\frac{8(0.9D)}{q}} k^z(\mathbf{X}^{tr}, \mathbf{x}^{ts})$
      $+ \left(\dfrac{q}{8(0.9D)}\right)^2 \mathbf{1}_{\frac{8(0.9D)}{q}\times\frac{8(0.9D)}{q}} \widetilde{\mathbf{K}}\mathbf{1}_{\frac{8(0.9D)}{q}\times 1}$.
      $p(\mathbf{x}^{ts}) \leftarrow \sum_{i=1}^{\frac{q}{8(0.9D)}} \mathbf{w}_n \widetilde{\mathbf{K}}^z(\mathbf{x}^{ts})$.
      $\hat{\mathbf{Y}}^s \leftarrow \left[\hat{\mathbf{Y}}^s,\ \hat{y} \leftarrow \begin{cases} 1, & p(\mathbf{x}^{ts}) \geq b^s, \\ 2, & p(\mathbf{x}^{ts}) < b^s. \end{cases}\right]$
    end for
    $\text{Acc}^s \leftarrow$ Accuracy with $(\mathbf{Y}^{ts}, \hat{\mathbf{Y}}^{sT})$.
  end for
  $A_z \leftarrow \dfrac{1}{q}\sum_{s=1}^{q} \text{Acc}^s$; $b_z \leftarrow \dfrac{1}{q}\sum_{s=1}^{q} b^s$.
end for
$z^* \leftarrow \arg\max_z A_z$; $A^* \leftarrow A_{z^*}$.
$(w^*, b^*) \leftarrow$ recompute with z^* using $(\mathbf{X}_{TR}, \mathbf{Y}_{TR})$.
$p(\mathbf{x}) \leftarrow \sum_{n=1}^{|\mathbf{X}_{TR}|} w_n^* k^{z^*}(\mathbf{x}_n, \mathbf{x}), \quad \mathbf{x} \in \mathbf{X}_{TS}$.
$\widehat{\mathbf{Y}} \leftarrow \left[\begin{cases} 1, & p(\mathbf{x}) \geq b^*, \\ 2, & p(\mathbf{x}) < b^*. \end{cases}\right]$
$A_t \leftarrow$ Accuracy with $(\mathbf{Y}_{TS}, \hat{\mathbf{Y}}^T)$.
$\mathbf{S} \leftarrow$ confusion matrix with $(\mathbf{Y}_{TS}, \hat{\mathbf{Y}}^T)$.

Algorithm A2 Used to estimate the parameters measured by IOSs

Require: $\mathbf{X} \leftarrow \mathbf{X}^T, \mathbf{Y}, \alpha, z, k^z(\cdot,\cdot)$
Ensure: $\alpha^*, z^*, RMSE^*, MAE^*, (R^2)^*, RMSE_t, MAE_t, (R^2)_t, \hat{\mathbf{Y}}$

$q = 5$.
$(\mathbf{X}, \mathbf{Y}) \xrightarrow{\text{90/10 split}} [(\mathbf{X}_{TR}, \mathbf{Y}_{TR}), (\mathbf{X}_{TS}, \mathbf{Y}_{TS})]$.
$\mathbf{X}_{TR} \xrightarrow{\text{q-fold}} [\mathbf{fold}_1^{\mathbf{X}}\ \mathbf{fold}_2^{\mathbf{X}}\ \ldots\ \mathbf{fold}_q^{\mathbf{X}}]$.
$\mathbf{Y}_{TR} \xrightarrow{\text{q-fold}} [\mathbf{fold}_1^{\mathbf{Y}}\ \mathbf{fold}_2^{\mathbf{Y}}\ \ldots\ \mathbf{fold}_q^{\mathbf{Y}}]$.
$\mathrm{RMSE}^{z,\alpha}, \mathrm{MAE}^{z,\alpha}, (R^2)^{z,\alpha} \leftarrow [\,]$.
for each $z \in \{0, m, 2m, \ldots, 1\}$ **do**
  for each $\alpha \in \{0, m, 2m, \ldots, 1\}$ **do**
    $RMSE \leftarrow 0; \quad MAE \leftarrow 0; \quad R^2 \leftarrow 0.$
    for each $s \in \{1, \ldots, q\}$ **do**
      $\mathbf{X}^{tr} \leftarrow \cup_{j \neq s} \mathbf{fold}_j^{\mathbf{X}}; \quad \mathbf{X}^{ts} \leftarrow \mathbf{fold}_s^{\mathbf{X}}.$
      $\mathbf{Y}^{tr} \leftarrow \cup_{j \neq s} \mathbf{fold}_j^{\mathbf{Y}}; \quad \mathbf{Y}^{ts} \leftarrow \mathbf{fold}_s^{\mathbf{Y}}.$
      $\mathbf{X}^{tr} \leftarrow \dfrac{\mathbf{X}^{tr} - \mathrm{mean}(\mathbf{X}^{tr})}{\mathrm{std}(\mathbf{X}^{tr})}; \quad \mathbf{X}^{ts} \leftarrow \dfrac{\mathbf{X}^{ts} - \mathrm{mean}(\mathbf{X}^{tr})}{\mathrm{std}(\mathbf{X}^{tr})}.$
      for each $\mathbf{x}^{tr} \in \mathbf{X}^{tr}$ **do**
        $(\mathbf{K}_s)_{nm} \leftarrow k^z(\mathbf{x}_n^{tr}, \mathbf{x}_m^{tr}).$
      end for
      $\boldsymbol{\beta}_s \leftarrow (\mathbf{K}_s + \alpha \mathbf{I})^{-1} \mathbf{Y}^{tr}; \quad \hat{\mathbf{Y}}^{ts} \leftarrow [\,].$
      for each $\mathbf{x}^{ts} \in \mathbf{X}^{ts}$ **do**
        $\boldsymbol{\theta} \leftarrow k^z(\mathbf{x}^{ts}, \mathbf{X}^{tr}).$
        $\hat{\mathbf{Y}}^{ts} \leftarrow [\hat{\mathbf{Y}}^{ts}, \boldsymbol{\theta}\boldsymbol{\beta}_s].$
      end for
      $RMSE_s \leftarrow \sqrt{\dfrac{1}{0.18D}(\mathbf{Y}^{ts} - \hat{\mathbf{Y}}^{ts})^T(\mathbf{Y}^{ts} - \hat{\mathbf{Y}}^{ts})}.$
      $MAE_s \leftarrow \dfrac{1}{0.18D} \sum_{i=1}^{0.18D} \left| y_i^{ts} - \hat{y}_i^{ts} \right|.$
      $(R^2)_s \leftarrow 1 - \dfrac{\sum_{i=1}^{0.18D} \left(y_i^{ts} - \hat{y}_i^{ts}\right)^2}{\sum_{i=1}^{0.18D} \left(y_i^{ts} - \bar{y}^{ts}\right)^2}.$
      $RMSE \leftarrow RMSE + RMSE_s;$
      $MAE \leftarrow MAE + MAE_s;$
      $R^2 \leftarrow R^2 + (R^2)_s.$
    end for
    $\mathrm{RMSE}^{z,\alpha} \leftarrow [\mathrm{RMSE}^{z,\alpha}\ \mathrm{RMSE}/q].$
    $\mathrm{MAE}^{z,\alpha} \leftarrow [\mathrm{MAE}^{z,\alpha}\ \mathrm{MAE}/q].$
    $(R^2)^{z,\alpha} \leftarrow [(R^2)^{z,\alpha}\ R^2/q].$
  end for
end for
$(z^*, \alpha^*) \leftarrow \arg\min_{z,\alpha} RMSE^{z,\alpha}.$
$RMSE^* \leftarrow RMSE^{z^*,\alpha^*}.$
$MAE^* \leftarrow MAE^{z^*,\alpha^*}$
$(R^2)^* \leftarrow (R^2)^{z^*,\alpha^*}.$
Apply steps 12–20 to $(\mathbf{X}_{TR}, \mathbf{Y}_{TR})$ using z^*, α^* and predict $\mathbf{X}_{TS}$ to obtain $\hat{\mathbf{Y}}$.
$RMSE_t \leftarrow \sqrt{\dfrac{1}{(0.1D)}(\mathbf{Y}_{TS} - \hat{\mathbf{Y}})^T(\mathbf{Y}_{TS} - \hat{\mathbf{Y}})}.$
$MAE_t \leftarrow \dfrac{1}{0.1D} \sum_{i=1}^{0.1D} \left| y_i^{TS} - \hat{y}_i^{TS} \right|.$
$(R^2)_t \leftarrow 1 - \dfrac{\sum_{i=1}^{0.1D} \left(y_i^{TS} - \hat{y}_i^{TS}\right)^2}{\sum_{i=1}^{0.1D} \left(y_i^{TS} - \bar{y}^{TS}\right)^2}.$

References

1. Wang, Y.; Yuan, W.; Yan, Y.; Lian, Z.; Chen, D.; Lau, A.P.T.; Yu, C.; Lu, C. Signal processing integrated with fiber-optic Vernier effect for the simultaneous measurement of relative humidity and temperature. *Opt. Express* **2023**, *31*, 28636–28648. [CrossRef]
2. Dai, X.; Wang, S.; Jiang, J.; Yang, H.; Tan, K.; Li, Z.; Liu, T. High-sensitive MEMS Fabry–Perot pressure sensor employing an internal-external cavity Vernier effect. *Opt. Express* **2022**, *30*, 31840–31851. [CrossRef]
3. Quan, M.; Tian, J.; Yao, Y.; Yin, Z.; Zhou, X.; Yan, X.; Zhao, Y.; Cheng, T. Ultra-High Sensitivity Fabry–Perot Interferometer Gas Refractive Index Fiber Sensor Based on Photonic Crystal Fiber and Vernier Effect. *Opt. Lett.* **2015**, *40*, 4891–4894. [CrossRef]
4. Martínez-Manuel, R.; Valentín-Coronado, L.M.; Esquivel-Hernández, J.; Monga, K.J.-J.; LaRochelle, S. Machine learning implementation for unambiguous refractive index measurement using a self-referenced fiber refractometer. *IEEE Sens.* **2022**, *22*, 14134–14141. [CrossRef]
5. Li, H.; Li, K.; Li, H.; Meng, F.; Lou, X.; Zhu, L. Recognition and classification of FBG reflection spectrum under non-uniform field based on support vector machine. *Opt. Fiber Technol.* **2020**, *60*, 102371. [CrossRef]
6. Esquivel-Hernández, J.; Martínez-Manuel, R.; Valentín-Coronado, L.M.; Barrera, D.; Sales, S. Pattern-recognition-based dual-point fiber temperature sensor using a reliable synthetic database. *IEEE Sens. J.* **2024**, *24*, 7850–7857. [CrossRef]
7. Valentín-Coronado, L.M.; Martínez-Manuel, R.; Esquivel-Hernández, J.; Diaz, S.; Martínez-Guerrero, M.A.; Armendariz, M.A Vector-based pattern recognition algorithm for interferometric fiber sensor-signals analysis. *IEEE Photon. Technol. Lett.* 2025, *early access*. [CrossRef]
8. Vargas-Rodriguez, E.; Guzman-Chavez, A.D. Application of the generalized linear model to enable refractive index measurement with thermal sensitive interferometric sensors. *Opt. Commun.* **2022**, *524*, 128765. [CrossRef]
9. Mei, Y.; Xia, T.; Cai, H.; Liu, Z. Deep learning improved spectral demodulation of interferometry Vernier effect for pressure sensing. *J. Lightwave Technol.* **2024**, *42*, 430–440. [CrossRef]
10. Mei, Y.; Zhang, S.; Cao, Z.; Xia, T.; Yi, X.; Liu, Z. Deep learning assisted pressure sensing based on Sagnac interferometry realized by side-hole fiber. *J. Lightwave Technol.* **2022**, *41*, 784–793. [CrossRef]
11. Dey, K.; Nikhil, V.; Roy, S. Machine learning approach with higher accuracy for simultaneous measurement of dual parameters using MSM fiber structure. *Measurement* **2023**, *221*, 113426. [CrossRef]
12. Zhao, Y.; Zhou, Y.; Ren, L.; Zhao, J.; Lv, R.; Zhang, Y.-N. Machine learning assisted fast demodulation of large dynamic range dual-parameter optical fiber sensors. *IEEE Sens. J.* **2023**, *23*, 31440–31446. [CrossRef]
13. Naku, W.; Alsalman, O.; Zhu, C. High-sensitivity and large-range displacement sensor based on a balloon-shaped optical fiber and machine learning analysis. *J. Lightwave Technol.* **2024**, *42*, 5399–5406. [CrossRef]
14. Djurhuus, M.S.; Werzinger, S.; Schmauss, B.; Clausen, A.T.; Zibar, D. Machine learning assisted fiber Bragg grating-based temperature sensing. *IEEE Photon. Technol. Lett.* **2019**, *31*, 939–942. [CrossRef]
15. Gallegos-Arellano, E.; Vargas-Rodriguez, E.; Guzman-Chave, A.D.; Cano-Contreras, M.; Cruz, J.L.; Raja-Ibrahim, R.K. Finely tunable laser based on a bulk silicon wafer for gas sensing applications. *Laser Phys. Lett.* **2016**, *13*, 065102. [CrossRef]
16. Schölkopf, B.; Smola, A.J. *Learning with Kernels: Support Vector Machines, Regularization, Optimization, and Beyond*; MIT Press: Cambridge, MA, USA, 2001. [CrossRef]
17. Kung, S.Y. *Kernel Methods and Machine Learning*; Cambridge University Press: Cambridge, UK, 2014. [CrossRef]
18. Vargas-Rodriguez, E.; Guzman-Chavez, A.D.; Raja-Ibrahim, R.K. Determination of the nonlinear thermal expansion coefficient of an epoxy used as an expander and its effects over a Fabry-Perot cavity filled with a polymer. *Opt. Mater. Express.* **2024**, *14*, 2054–2064. [CrossRef]
19. Vargas-Rodriguez, E.; Guzman-Chavez, A.D.; Garcia-Ramirez, M.A. Tunable Optical Filter Based on Two Thermal Sensitive Layers. *IEEE Photonics Technol.* **2018**, *30*, 1776–1779. [CrossRef]

Disclaimer/Publisher's Note: The statements, opinions and data contained in all publications are solely those of the individual author(s) and contributor(s) and not of MDPI and/or the editor(s). MDPI and/or the editor(s) disclaim responsibility for any injury to people or property resulting from any ideas, methods, instructions or products referred to in the content.